

# Quasi-equilibrium Binary Black Hole Initial Data for Dynamical Evolutions

Hwei-Jang Yo<sup>1,2</sup>, James N. Cook<sup>1</sup>, Stuart L. Shapiro<sup>1,3</sup>, and Thomas W. Baumgarte<sup>4,1</sup>

<sup>1</sup>*Department of Physics, University of Illinois at Urbana-Champaign, Urbana, Illinois 61801*

<sup>2</sup>*Institute of Astronomy and Astrophysics, Academia Sinica, Taipei 115, Taiwan, Republic of China*

<sup>3</sup>*Department of Astronomy & NCSA, University of Illinois at Urbana-Champaign, Urbana, Illinois 61801*

<sup>4</sup>*Department of Physics and Astronomy, Bowdoin College, Brunswick, Maine 04011*

We present a formalism for constructing quasi-equilibrium binary black hole initial data suitable for numerical evolution. We construct quasi-equilibrium models by imposing an approximate helical Killing symmetry appropriate for quasi-circular orbits. We use the sum of two Kerr-Schild metrics as our background metric, thereby improving on conformally flat backgrounds that do not accommodate rotating black holes and providing a horizon-penetrating lapse, convenient for implementing black hole excision. We set inner boundary conditions at an excision radius well inside the apparent horizon and construct these boundary conditions to incorporate the quasi-equilibrium condition and recover the solution for isolated black holes in the limit of large separation. We use our formalism both to generate initial data for binary black hole evolutions and to construct a crude quasi-equilibrium, inspiral sequence for binary black holes of fixed irreducible mass.

PACS numbers: 04.20.Ex, 04.25.Dm, 04.30.Db, 04.70.Bw, 95.30.Sf

## I. INTRODUCTION

The coalescence and merger of binary black holes is expected to be one of the primary sources of gravitational radiation to be detected by interferometric gravitational wave detectors (including the Laser Interferometer Gravitational Wave Observatory, LIGO, and the Laser Interferometer Space Antenna, LISA). The detection and interpretation of black hole mergers will be greatly facilitated by theoretical predictions for the gravitational waveforms produced by these events.

For large binary separations, post-Newtonian approximations can be used to model the binary inspiral and gravitational wave emission to excellent accuracy [1]. For small binary separations, when finite size and non-linear effects become more important, it is expected that numerical relativity simulations will provide the most accurate models and wave form predictions.

Constructing numerical models of the binary inspiral typically proceeds in two steps (see, e.g. [2] for a recent review). In the first step, initial data are constructed by solving the constraint equations of general relativity. These initial data, which provide a snapshot of the gravitational fields at a certain instant of time, are not unique, and certain freely specifiable functions have to be chosen in accordance with the astrophysical situation at hand (see also the review [3]). In the second step, the initial data are evolved dynamically forward in time, which provides the subsequent binary evolution and with it the emitted gravitational wave signal.

To date neither one of these two steps has been solved completely satisfactorily. A number of groups have constructed initial data describing binary black holes in nearly circular orbit [4, 5, 6, 7, 8, 9, 10, 11], and there have been several attempts at dynamical simulations of binary black holes [12, 13, 14, 15, 16]. While this effort has made significant progress, the numerical modeling of binary black hole inspiral remains an unsolved theoretical

problem.

Building on the success of the BSSN formulation of the evolution equations of general relativity [17, 18], we have recently developed a code that can stably evolve single, rotating black holes for arbitrary long times [19]. This code adopts a simple excision scheme [20] to remove the black hole deep interior and its singularities from the numerical grid. Implementation of such a scheme requires a coordinate system that smoothly extends into the black hole interior (“horizon-penetrating coordinates”), as for example Kerr-Schild coordinates (see [21, 22]). Our goal is to use this code for dynamical simulations of binary black hole systems in corotating coordinates. This requires initial data that describe binary black holes in quasi-circular orbit in horizon-penetrating coordinates.

The first models of binary black holes in quasi-circular orbits [4, 5] adopted the Bowen-York decomposition of the constraint equations [23]. When combined with maximal slicing and conformal flatness, the momentum constraints can be solved analytically, and only the Hamiltonian constraint needs to be solved numerically. For generalization to spinning black holes (compare [8]) it may be desirable to abandon conformal flatness. A recent spectral implementation by [11] shows that in the extreme mass ratio limit this approach does not recover the Schwarzschild test particle result, which underlines the need for alternative solutions. Furthermore, this approach only provides the initial data for the gravitational fields, and a suitable coordinate system for a subsequent evolution has yet to be chosen. Clearly, it is desirable to choose a rotating coordinate system in which the binary appears approximately static (i.e. a coordinate system that is based on the existence of an approximate helical Killing vector). Such a coordinate system is constructed in [24]. However, this coordinate system is not horizon-penetrating, since the lapse is not strictly positive. This is undesirable for the dynamical evolution and singularity excision (but see [16]; compare [25]).

An alternative approach, [6, 7] adopted a conformal thin-sandwich decomposition of the constraint equations [3, 26, 27] instead of the Bowen-York decomposition. This approach seems more appealing for the construction of quasi-equilibrium initial data, since it allows for the explicit specification of the time derivatives of the conformally related metric and the trace of the extrinsic curvature (see also [24, 28, 29].) In addition, this approach automatically provides a coordinate system that reflects quasi-equilibrium. In [6, 7], this decomposition was combined with the conformal-imaging approach of [4]. In addition to leading to some inconsistencies on the black hole throats (compare [30]) this again yields a lapse that is not strictly positive. Attempts to combine the thin-sandwich decomposition with a puncture approach [5, 31] fail because of mutually exclusive requirements between the different methods [25].

In this paper we borrow various ideas and approaches from previous investigators to construct initial data that are better suitable for evolution with our dynamical evolution code. In particular, we adopt the thin-sandwich decomposition of the constraint equations together with Kerr-Schild background data. In contrast to [28] we set the time derivative of the trace of the extrinsic curvature to zero, which we believe will result in data that are closer to quasi-equilibrium. On the excision surface we impose a boundary condition that is derived from requiring that the time derivative of the conformal factor vanish there. We impose circular orbits by setting the ADM mass equal to the Komar mass, which is equivalent to imposing a relativistic virial theorem [6, 7] (see also [10, 32].)

We solve these equations numerically by finite differencing in Cartesian coordinates, which leads to results that are less accurate than those achieved with spectral methods (compare [28]), but better suited for evolutions with our dynamical code, which also uses finite differencing and Cartesian coordinates. The accuracy requirements for initial data are much less stringent than those for constructing accurate quasi-equilibrium sequences, which are typically determined from small differences between large numbers. As a by-product of our calculations, we nevertheless present a crude inspiral, quasi-equilibrium binary sequence.

The paper is organized as follows. In Section II we review the basic equations, boundary conditions and the construction of quasi-circular orbits. We present numerical results in Section III, and we discuss our findings in Section IV. We also include several Appendices with specifics of our numerical implementation.

## II. BASIC EQUATIONS

### A. The Thin-Sandwich Equations

We begin by writing the metric in the ADM form

$$ds^2 = -\alpha^2 dt^2 + \gamma_{ij}(dx^i + \beta^i dt)(dx^j + \beta^j dt), \quad (1)$$

where  $\alpha$  is the lapse function,  $\beta^i$  is the shift vector, and  $\gamma_{ij}$  is the spatial metric. Throughout this paper, Latin indices are spatial indices and run from 1 to 3, whereas Greek indices are spacetime indices and run from 0 to 3.

The Einstein equations can then be decomposed into the Hamiltonian constraint  $\mathcal{H}$  and the momentum constraint  $\mathcal{M}_i$

$$\mathcal{H} \equiv R - K_{ij}K^{ij} + K^2 = 0, \quad (2)$$

$$\mathcal{M}^i \equiv \nabla_j K^{ij} - \nabla^i K = 0, \quad (3)$$

and the evolution equations

$$\partial_t \gamma_{ij} = -2\alpha K_{ij} + \nabla_i \beta_j + \nabla_j \beta_i. \quad (4)$$

$$\begin{aligned} \partial_t K_{ij} = & \alpha (R_{ij} - 2K_{i\ell}K_j^\ell + K K_{ij}) - \nabla_i \nabla_j \alpha \\ & + \beta^\ell \nabla_\ell K_{ij} + K_{i\ell} \nabla_j \beta^\ell + K_{j\ell} \nabla_i \beta^\ell, \end{aligned} \quad (5)$$

Here we have assumed a vacuum spacetime ( $T_{\alpha\beta} = 0$ ), and  $\nabla_i$ ,  $R_{ij}$  and  $R \equiv \gamma^{ij}R_{ij}$  are the covariant derivative, the Ricci tensor and scalar curvature associated with the spatial metric  $\gamma_{ij}$ . The extrinsic curvature  $K_{ij}$  is defined by equation (4).

Most decompositions of the constraint equations start with a York-Lichnerowicz conformal decomposition of the metric

$$\gamma_{ij} \equiv \psi^4 \tilde{\gamma}_{ij}, \quad (6)$$

where  $\psi$  is the conformal factor and  $\tilde{\gamma}_{ij}$  the conformally related metric [33, 34]. It is also useful to decompose the extrinsic curvature  $K_{ij}$  into its trace  $K$  and a tracefree part  $A_{ij}$ ,

$$K_{ij} \equiv A_{ij} + \frac{1}{3}\gamma_{ij}K, \quad (7)$$

and to conformally transform  $A_{ij}$  according to

$$A^{ij} \equiv \psi^{-10} \tilde{A}^{ij} \quad (8)$$

(so that  $A_{ij} = \psi^{-2} \tilde{A}_{ij}$ ; see [35, 36].) With these definitions the Hamiltonian constraint (2) becomes

$$\tilde{\nabla}^2 \psi - \frac{1}{8}\psi \tilde{R} - \frac{1}{12}\psi^5 K^2 + \frac{1}{8}\psi^{-7} \tilde{A}_{ij} \tilde{A}^{ij} = 0, \quad (9)$$

where  $\tilde{\nabla}_i$  and  $\tilde{R}$  are the covariant derivative and scalar curvature associated with  $\tilde{\gamma}_{ij}$ , and  $\tilde{\nabla}^2 \equiv \tilde{\nabla}^i \tilde{\nabla}_i$  is the scalar Laplace operator.

For a complete derivation of the conformal thin-sandwich decomposition we refer the reader to references [26, 27, 37]. Here we focus on the construction of binary

black holes in quasi-equilibrium. In a corotating coordinate system one expects the gravitational field to depend on time only very weakly, and it is therefore natural to construct initial data for which as many functions as possible have vanishing time derivative. Within the conformal thin-sandwich formalism both the time derivative of the conformally related metric and the extrinsic curvature appear as freely specifiable data, and it is therefore both possible and natural to set

$$\partial_t K = 0 \quad (10)$$

and

$$\partial_t \tilde{\gamma}_{ij} = 0. \quad (11)$$

Inserting the latter into (4) we obtain

$$\tilde{A}^{ij} = \frac{\psi^6}{2\alpha} \left( (\tilde{\mathbb{L}}\beta)^{ij} \right). \quad (12)$$

where

$$(\tilde{\mathbb{L}}X)^{ij} \equiv \tilde{\nabla}^i X^j + \tilde{\nabla}^j X^i - \frac{2}{3} \tilde{\gamma}^{ij} \tilde{\nabla}_\ell X^\ell. \quad (13)$$

Equation (12) can now be inserted into the Momentum constraint (3), which yields

$$\tilde{\Delta}_\perp \beta^i - (\tilde{\mathbb{L}}\beta)^{ij} \tilde{\nabla}_j \ln \left( \frac{\alpha}{\psi^6} \right) = \frac{4}{3} \alpha \tilde{\nabla}^i K,$$

where

$$\tilde{\Delta}_\perp \beta^i = \tilde{\nabla}_j (\tilde{\mathbb{L}}\beta)^{ij} = \tilde{\nabla}^2 \beta^i + \frac{1}{3} \tilde{\nabla}^i (\tilde{\nabla}_j \beta^j) + \tilde{R}^i_j \beta^j. \quad (14)$$

Finally, condition (10) can be inserted into the trace of the evolution equation (5), which, after combining with the Hamiltonian constraint (9) becomes

$$\begin{aligned} \tilde{\nabla}^2(\alpha\psi) - \alpha \left( \frac{1}{8} \psi \tilde{R} + \frac{5}{12} \psi^5 K^2 \right. \\ \left. + \frac{7}{8} \psi^{-7} \tilde{A}_{ij} \tilde{A}^{ij} \right) = \psi^5 \beta^i \tilde{\nabla}_i K, \end{aligned} \quad (15)$$

To summarize, the thin-sandwich formalism then provides three equations

$$\tilde{\Delta}_\perp \beta^i - (\tilde{\mathbb{L}}\beta)^{ij} \tilde{\nabla}_j \ln \left( \frac{\alpha}{\psi^6} \right) - \frac{4}{3} \alpha \tilde{\nabla}^i K = 0 \quad (16)$$

$$\tilde{\nabla}^2 \psi - \frac{1}{8} \psi \tilde{R} - \frac{1}{12} \psi^5 K^2 + \frac{1}{8} \psi^{-7} \tilde{A}_{ij} \tilde{A}^{ij} = 0 \quad (17)$$

$$\begin{aligned} \tilde{\nabla}^2(\alpha\psi) - (\alpha\psi) \left[ \frac{1}{8} \tilde{R} + \frac{5}{12} \psi^4 K^2 \right. \\ \left. + \frac{7}{8} \psi^{-8} \tilde{A}_{ij} \tilde{A}^{ij} \right] = \psi^5 \beta^i \tilde{\nabla}_i K, \end{aligned} \quad (18)$$

for the three unknowns  $\alpha$ ,  $\beta^i$  and  $\psi$ . The tracefree part of the extrinsic curvature is related to these unknowns through equation (12). Before the equations can be solved, a background geometry  $\tilde{\gamma}_{ij}$  and a background trace of the extrinsic curvature  $K$  has to be chosen.

## B. Kerr-Schild Background Data

We base our choice for the freely specifiable data on a superposition of two Kerr black holes in Kerr-Schild coordinates [21, 22, 28]. A Kerr-Schild metric is given by

$$g_{\mu\nu} = \eta_{\mu\nu} + 2H l_\mu l_\nu, \quad (19)$$

where  $\eta_{\mu\nu}$  is the Minkowski metric, and  $l_\mu$  is a null-vector with respect to both the full metric and the Minkowski metric,  $g^{\mu\nu} l_\mu l_\nu = \eta^{\mu\nu} l_\mu l_\nu = 0$ . From the spacetime metric (19) the spatial metric, the lapse and the shift can be identified as

$$\gamma_{ij} = \delta_{ij} + 2H l_i l_j, \quad (20)$$

$$\alpha = (1 + 2H l^t l^t)^{-1/2}, \quad (21)$$

$$\beta^i = -\frac{2H l^t l^i}{1 + 2H l^t l^t}. \quad (22)$$

For a black hole of mass  $M$  and angular momentum  $M\vec{a}$  at rest at the origin,  $H$  and  $l_\mu$  are given by

$$H = \frac{Mr^3}{r^4 + (\vec{a} \cdot \vec{x})^2}, \quad (23)$$

$$l_\mu = (1, \vec{l}), \quad (24)$$

$$\vec{l} = \frac{r\vec{x} - \vec{a} \times \vec{x} + (\vec{a} \cdot \vec{x})\vec{a}/r}{r^2 + a^2}, \quad (25)$$

with

$$r^2 = \frac{\vec{x}^2 - \vec{a}^2}{2} + \left( \frac{\vec{x}^2 - \vec{a}^2}{4} + (\vec{a} \cdot \vec{x})^2 \right)^{1/2}. \quad (26)$$

For a non-rotating black hole with  $\vec{a} = 0$ ,  $H$  has a pole at the origin, whereas for rotating black holes  $H$  has a ring singularity. We therefore have to excise from the computational domain a region enclosing the singularity. In this paper we adopt a non-spinning Kerr-Schild background to describe co-rotating black hole binaries in a co-rotating frame.

We want to generate initial data for a spacetime containing two black holes with background masses  $M_A$  and  $M_B$ , velocities  $\vec{v}_A$  and  $\vec{v}_B$ , and we will assume that the background metric has zero spin  $M\vec{a}$ . Such initial data can be constructed by adopting for the freely specifiable background data a superposition of two Kerr-Schild coordinate systems describing two individual black holes [21, 22]. The first black hole with label A has a spatial metric

$$\gamma_{Aij} = \delta_{ij} + 2H_A l_{Ai} l_{Aj}, \quad (27)$$

an extrinsic curvature  $K_{Aij}$ , a lapse  $\alpha_A$  and a shift  $\beta_A^i$ . The trace of the extrinsic curvature is

$$K_A = \frac{2M_A}{r_A^2 (1 + 2M_A/r_A)^{3/2}} (1 + 3M_A/r_A). \quad (28)$$

The second black hole has a similar set of associated quantities which are labeled with the letter B.

In Section II A we have already adopted  $\partial_t \tilde{\gamma}_{ij} = 0$  and  $\partial_t K = 0$ , which leaves as the freely specifiable background quantities the background metric  $\tilde{\gamma}_{ij}$  and the trace of the extrinsic curvature  $K$ , for which we choose the “superpositions”

$$\tilde{\gamma}_{ij} = \delta_{ij} + 2H_A l_{A i} l_{A j} + 2H_B l_{B i} l_{B j} \quad (29)$$

and

$$K = K_A + K_B. \quad (30)$$

### C. Outer Boundary Conditions

The requirement of corotation and the conditions of asymptotic flatness yield boundary conditions at spatial infinity

$$\psi|_{r \rightarrow \infty} = 1, \quad (31)$$

$$\beta^i|_{r \rightarrow \infty} = \Omega(\partial_\phi)^i, \quad (32)$$

$$\alpha|_{r \rightarrow \infty} = 1, \quad (33)$$

where  $\Omega$  is the angular velocity of the corotating frame. Since our computational domain does not extend to spatial infinity, we have to impose approximate boundary conditions at a finite separation. The asymptotic behavior of the metric in a binary black hole system is similar to that of any rotating system in an asymptotically flat spacetime, including a Kerr black hole. The asymptotic form of a Kerr black hole tells us the form of the leading-order, radial fall-off term of the shift that is important for determining the system’s angular momentum (via a quadrature over the extrinsic curvature in eqn. 53 below). To incorporate the angular momentum of the binary in the outer boundary condition of the shift vector, we consider the asymptotic shift of a single, *rotating* Kerr-Schild black hole and focus on the leading terms proportional to the spin. In our asymptotic binary shift we “correct” the shift associated with the non-spinning background metric with terms that have the same asymptotic fall-off as these spin-dependent terms. A similar argument for choosing the form of the asymptotic shift in our binary has been put forward in Sec. III E of [47].

For a single Kerr-Schild black hole we have

$$\begin{aligned} \beta^x &= \frac{2Mx}{r^2} + 2M \frac{-2Mx + ay}{r^3} + O(r^{-3}), \\ \beta^y &= \frac{2My}{r^2} + 2M \frac{-2My - ax}{r^3} + O(r^{-3}), \\ \beta^z &= \frac{2Mz}{r^2} - 4M^2 \frac{z}{r^3} + 2M \frac{(4M^2 + a^2)z}{r^4} + O(r^{-4}), \end{aligned} \quad (34)$$

where we have assumed rotation about the  $z$ -axis,  $\vec{a} = (0, 0, a)$ . Equation (34) suggests the following fall-off conditions at the edge of our computational grid for the binary:

$$\psi - 1 \sim \frac{1}{r}, \quad (35)$$

$$\beta^x - \bar{\beta}^x \sim \frac{y}{r^3}, \quad (36)$$

$$\beta^y - \bar{\beta}^y \sim \frac{x}{r^3}, \quad (37)$$

$$\beta^z - \bar{\beta}^z \sim \frac{z}{r^4}, \quad (38)$$

$$\alpha - 1 \sim \frac{1}{r}. \quad (39)$$

Here the boundary condition of the shift vector consists of an analytic part,  $\bar{\beta}^i$ , and a higher-order part.  $\bar{\beta}^i$  is the sum of the analytic shifts from each nonspinning black hole ( $a = 0$ ) plus  $(\vec{\Omega} \times \vec{r})^i$ , which accounts for all shift terms except for terms due to the orbital rotation (frame-dragging) as identified above. The *form* of the higher-order terms on the right-hand side comes from consideration of the way in which the system’s total angular momentum is embedded in the asymptotic shift, as we argued above. The *coefficients* for the higher-order terms are determined by numerically fitting to the data immediately interior to the boundary; they are not given a priori. Note that the shift in Sec IV A of [6] exhibits the same asymptotic behavior as in eqn. (36)-(38), including the higher-order, fall-off terms containing the angular momentum data. The boundary conditions of [6] and ours differ only in the analytical part: the background shift in [6] is based on isotropic coordinates, while in our approach it is based on Kerr-Schild coordinates. Apart from the background, the form for the leading-order terms, including the rotational terms, is the same in both calculations (compare eqns 36-38 in our paper with eqns 161-163 in [6]).

### D. Inner Boundary Conditions

Since the metric is singular at the center of each hole, some part of the black hole interior has to be excised from the computational domain, which introduces the need for inner boundary conditions. In [28] the following set of inner boundary conditions was adopted

$$\psi = 1 \quad \text{all boundaries}, \quad (40a)$$

$$\beta^i = \beta_A^i \quad \text{sphere inside hole A}, \quad (40b)$$

$$\beta^i = \beta_B^i \quad \text{sphere inside hole B}. \quad (40c)$$

Since [28] specified the lapse as either  $\alpha = \psi^6 \alpha_A \alpha_B$  or  $\alpha = \psi^6 (\alpha_A + \alpha_B - 1)$ , no boundary condition for the lapse was required. We solve equation (15) for the lapse, and therefore need an addition boundary condition.

The set of conditions (40) is very simple to implement, but does not necessarily lead to quasi-equilibrium solutions. Assuming that the black holes are equilibrium (or “isolated” in the language of [40]) Cook [30] derived an alternative set of boundary conditions (see also [41, 42]). Unfortunately, the resulting equations are quite complicated and difficult to implement numerically. We have therefore chosen to adopt an alternative set of boundary conditions, which is motivated by the observation that

for corotating, quasi-equilibrium black holes in a binary black hole system the time derivative

$$\partial_t \ln \sqrt{\gamma} = \nabla_i \beta^i - \alpha K \quad (41)$$

should be small [48].

For the lapse and shift we set

$$\alpha = \alpha_A \alpha_B \quad (42)$$

$$\beta^i = \alpha_A \beta_B^i + \alpha_B \beta_A^i \quad (43)$$

on the inner boundaries and note that these choices reduce to the correct values in the limit of infinite binary separation. Imposing inner boundary conditions somewhere inside the black hole horizon implicitly assumes that the solution should not depend on where exactly this condition is imposed. This suggests that the above condition should hold not only on the boundary itself, but, to a certain approximation, also in the neighborhood of the boundary. With our choices of the conformal metric

$$\gamma_{ij} = \psi^4 \tilde{\gamma}_{ij} = \psi^4 (\gamma_{ij}^A + \gamma_{ij}^B - \delta_{ij}) \quad (44)$$

and the trace of the extrinsic curvature

$$K = K_A + K_B. \quad (45)$$

we can then compute

$$\begin{aligned} & \nabla_i \beta^i - \alpha K \\ &= \nabla_i (\alpha_A \beta_B^i + \alpha_B \beta_A^i) - \alpha_A \alpha_B (K_A + K_B) \\ &= \partial_i (\alpha_A \beta_B^i + \alpha_B \beta_A^i) + \Gamma^j_{ji} (\alpha_A \beta_B^i + \alpha_B \beta_A^i) \\ &\quad - \alpha_A \alpha_B (K_A + K_B) \\ &= \alpha_A (\nabla_i^B \beta_B^i - \alpha_B K_B) + \alpha_B (\nabla_i^A \beta_A^i - \alpha_A K_A) \\ &\quad + \beta_B^i [\partial_i \alpha_A + \alpha_A (\Gamma^j_{ji} - {}_B \Gamma^j_{ji})] \\ &\quad + \beta_A^i [\partial_i \alpha_B + \alpha_B (\Gamma^j_{ji} - {}_A \Gamma^j_{ji})] \\ &= \beta_B^i [\partial_i \alpha_A + \alpha_A \partial_i \ln \sqrt{\gamma/\gamma_B}] \\ &\quad + \beta_A^i [\partial_i \alpha_B + \alpha_B \partial_i \ln \sqrt{\gamma/\gamma_A}] \\ &= \beta_B^i \alpha_A \partial_i \ln \sqrt{\gamma/\gamma_A \gamma_B} + \beta_A^i \alpha_B \partial_i \ln \sqrt{\gamma/\gamma_A \gamma_B} \\ &= \beta^i \partial_i \ln(\sqrt{\gamma} \alpha). \end{aligned} \quad (46)$$

Here we have used  $\nabla_i \beta^i - \alpha K = 0$  as well as  $\Gamma^j_{ji} = \partial_i \ln \sqrt{\gamma}$ ,  $\tilde{\Gamma}^j_{ji} = \partial_i \ln \sqrt{\tilde{\gamma}}$ , and  $\alpha = \gamma^{-1/2}$  for both background black holes  $A$  and  $B$ . With  $\gamma = \psi^{12} \tilde{\gamma}$ , equation (46) can be rewritten

$$\nabla_i \beta^i - \alpha K = \beta^i \partial_i \ln(\sqrt{\gamma} \alpha) = \beta^i \partial_i \ln(\alpha \psi^6 \sqrt{\tilde{\gamma}}). \quad (47)$$

According to (41) we expect  $\nabla_i \beta^i - \alpha K$  to be small, so that (46) becomes

$$6\beta^i \partial_i \psi + \psi \beta^i (\tilde{\Gamma}^j_{ji} + \partial_i \ln \alpha) = 0, \quad (48)$$

which provides a Neumann condition for the conformal factor on the inner boundary. Collecting the inner boundary conditions, we then have

$$\alpha = \alpha_A \alpha_B,$$

$$\begin{aligned} \beta^i &= \alpha_A \beta_B^i + \alpha_B \beta_A^i, \\ 6\beta^i \partial_i \psi &= -\psi \beta^i (\tilde{\Gamma}^j_{ji} + \partial_i \ln \alpha) \end{aligned} \quad (49)$$

In the limit of infinite separation each black hole reduces to an isolated Kerr-Schild black hole, which satisfies the above conditions.

### E. Constructing quasi-equilibrium circular orbits and sequences

Solving equations (16) – (18) subject to the boundary conditions (35) – (39) and (49) yields a solution describing two black holes at a particular separation  $d$ , mass  $M$  and angular momentum  $J$ . Sequences of constant irreducible mass binaries in circular orbit can be constructed as follows (see also the flow chart in Fig. 1).

Focusing on equal-mass binaries, we first choose a value of the irreducible mass  $M_{\text{irr}}$  [49, 50, 51], which remains constant during the slow, adiabatic binary inspiral (see also [7, 52]). The irreducible mass is determined from the area of the black hole event horizon, but in practice we approximate this value by computing the area of the apparent horizon

$$M_{\text{irr}} \approx \left( \frac{A}{16\pi} \right)^{1/2}. \quad (50)$$

We next choose a separation  $d$ , and begin the iteration with a trial value of the background masses  $M_A = M_B = M$ , which enters the background geometry  $\tilde{\gamma}_{ij}$  and  $K$ . We also choose a trial value of the orbital angular velocity  $\Omega$ , which enters the orbital shift in  $\tilde{\beta}^i$  in the outer boundary conditions (35) – (39). Solving equations (16) – (18) for these values will provide a binary that is not necessarily in circular orbit and does not necessarily have the required irreducible mass.

To impose circular orbits, we require that the system's ADM mass (e.g. [46])

$$M_{\text{ADM}} = \frac{1}{16\pi} \oint_{\infty} \gamma^{im} \gamma^{jn} (\gamma_{mn,j} - \gamma_{jn,m}) d^2 S_i, \quad (51)$$

be equal to its Komar mass [43]

$$M_K = \frac{1}{4\pi} \oint_{\infty} \gamma^{ij} (\nabla_i \alpha - \beta^k K_{ik}) d^2 S_j. \quad (52)$$

In the above expressions  $d^2 S_i = (1/2) \gamma^{1/2} \epsilon_{ijk} dx^j dx^k$  is the two-dimensional surface area element. In many cases,  $\beta^k K_{ik}$  falls off faster than  $O(r^{-2})$  in (52) so that the second term vanishes; in our case, however, this term cannot be neglected. We evaluate these integrals as described in Appendices A and B.

The equality of the ADM and Komar masses is closely related to a relativistic virial theorem [38] and indicates that the spacetime is stationary [44, 45] in the rotating frame. In [7] this criterion was adopted to impose circular orbits in binary black hole spacetimes (see also [32] for

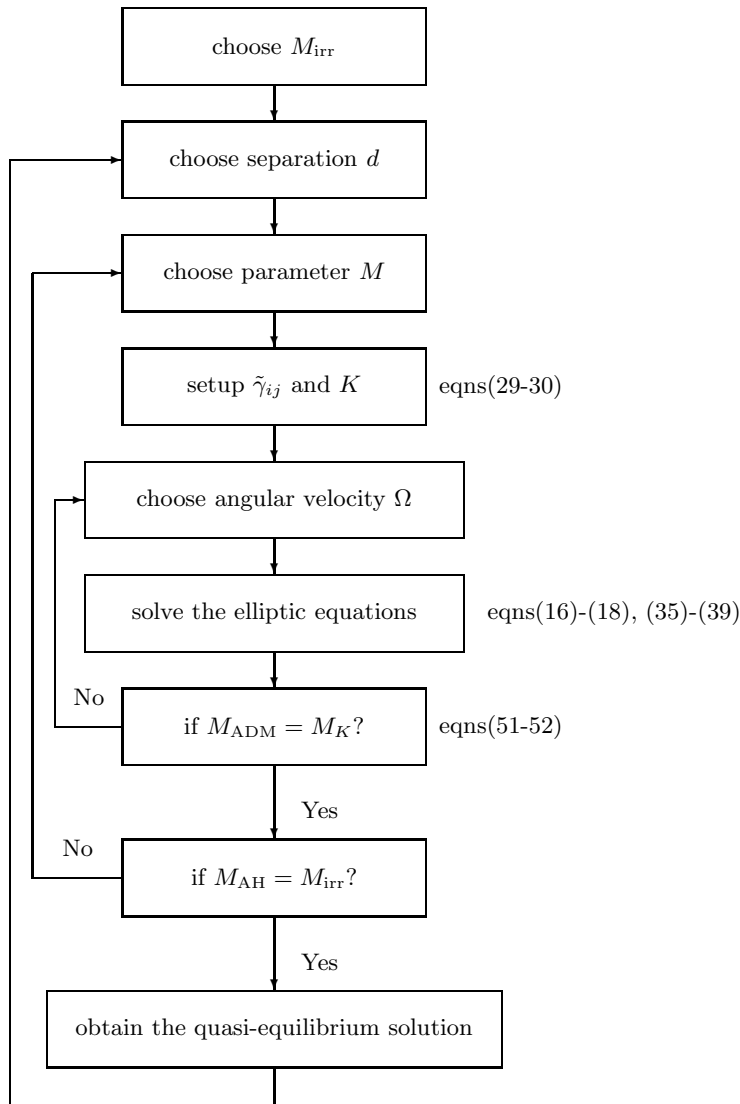


FIG. 1: Flow chart for the construction of sequences of quasi-equilibrium, circular-orbit binary black holes

a pedagogical illustration). In our code we iterate over  $\Omega$  until  $M_{\text{ADM}} = M_K$  has been achieved to within an accuracy of 1 part in  $10^6$ .

For a given circular orbit we then iterate over the background mass  $M$  until the irreducible mass  $M_{\text{irr}}$  has taken the desired value to within an accuracy of 1 part in  $10^6$  [53]. Finally we vary the binary separation  $d$  to construct an approximate inspiral sequence. For each model the ADM mass  $M_{\text{ADM}}$  is found from (51) and the angular momentum from

$$J_i = \frac{1}{8\pi} \epsilon_{ij}{}^k \oint_{\infty} x^j K^\ell{}_k d^2 S_\ell \quad (53)$$

(see Appendix C). The innermost stable circular orbit (ISCO) can be found by locating minima in the ADM mass and the angular momentum along a constant-mass sequence.

### III. NUMERICAL RESULTS

#### A. Tests

In this section we present two tests of our code. The first test shows second-order convergence to the analytic Kerr-Schild spacetime for a single black hole. The second test shows second-order convergence in a particular (non-equilibrium) binary solution previously considered by Pfeiffer [28].

##### 1. Single Black Hole Tests

To recover a single non-rotating black hole in Kerr-Schild coordinates we set  $M_B = 0$  and located the black hole  $A$  at the origin. We then solve equations (16) – (18)

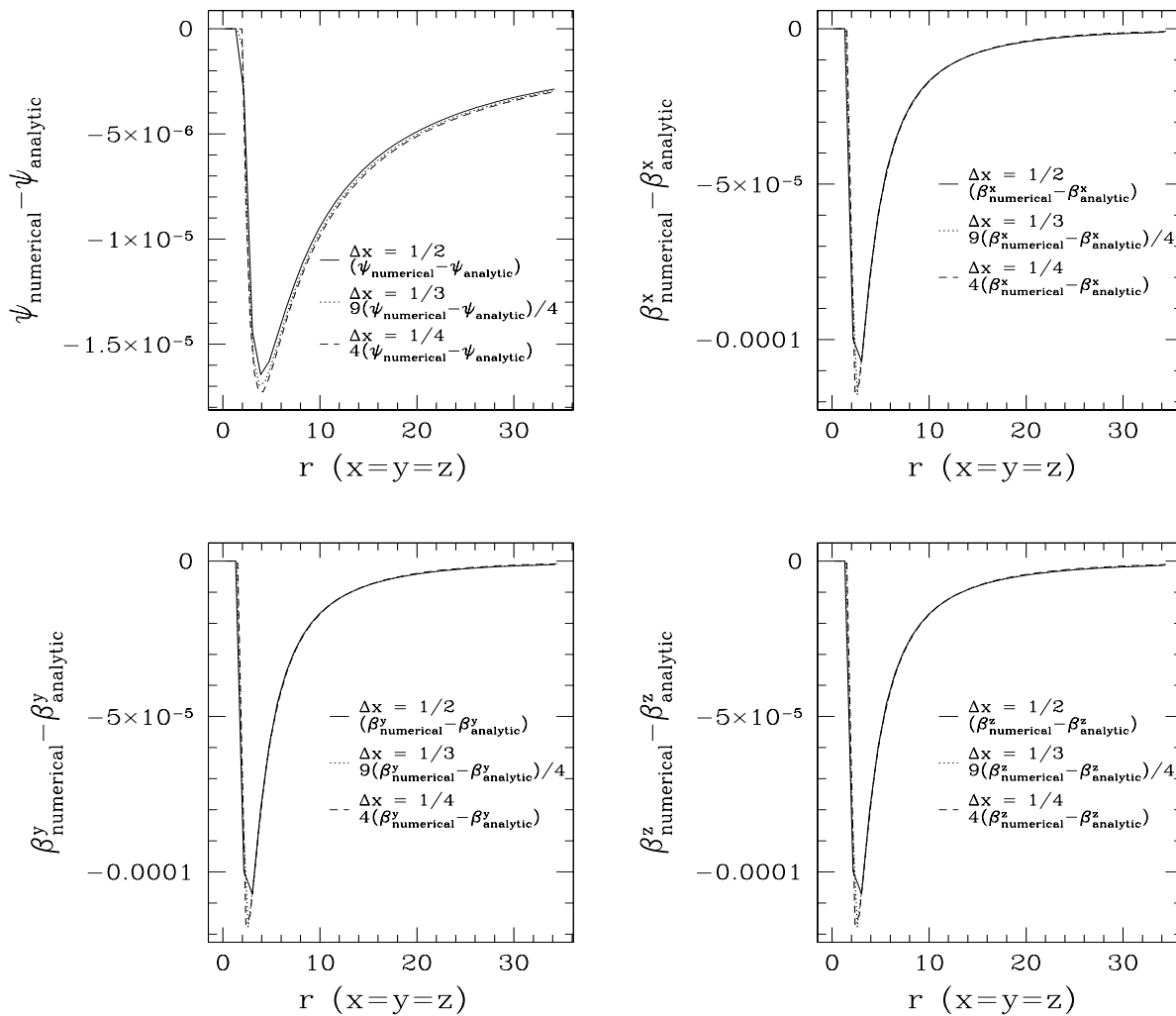


FIG. 2: Numerical errors in the conformal factor  $\psi$  and the shift  $\beta^i$  for three different resolutions  $\Delta x$  for a single, non-rotating Kerr-Schild black hole.

imposing Dirichlet inner boundary conditions

$$\begin{aligned} \psi &= 1, \\ \beta^i &= -\frac{2Hl^t l^i}{1 + 2Hl^t l^t}, \\ \alpha &= \frac{1}{\sqrt{1 + 2Hl^t l^t}} \end{aligned} \quad (54)$$

on a sphere of radius  $r_{\text{excision}} = 1.8M_0$ , where  $M_0$  is the background mass of one of our black holes at infinite separation. We run these tests with the IBM pSeries 690 machine in NCSA. A typical run with  $160 \times 80 \times 80$  grid-points takes about 16 cpu hours and uses about two giga bytes of memory. In Fig. 2 we show numerical errors for the conformal factor  $\psi$  and the shift  $\beta^i$  for several different resolutions. The errors scale as expected, establishing second-order convergence of our code. We chose to impose the above Dirichlet condition for  $\psi$  instead of the inner boundary condition (49) because, in our nu-

merical implementations, Dirichlet conditions are easier to impose at a fixed physical location, which is mandatory for achieving second-order convergence. For a resolution of  $\Delta x/M_0 = 1/6$  and with the outer boundary at  $20M_0$ , we find  $J/M_0^2 < 10^{-8}$ ,  $M_{\text{ADM}}/M_0 = 0.9990$ , and  $M_{\text{AH}} = 1.0013$ , which shows that the error in our solution is of the order of a fraction of a percent.

## 2. Comparison with a Previous Binary Black Hole Calculation

In this Section we compare with numerical results by Pfeiffer, Cook and Teukolsky [28] (hereafter PCT), who used spectral methods to construct black hole binaries. PCT solve equations (16) and (18), but instead of solving (17) for the lapse they experiment with two different choices for an analytic densitized lapse function. Here we

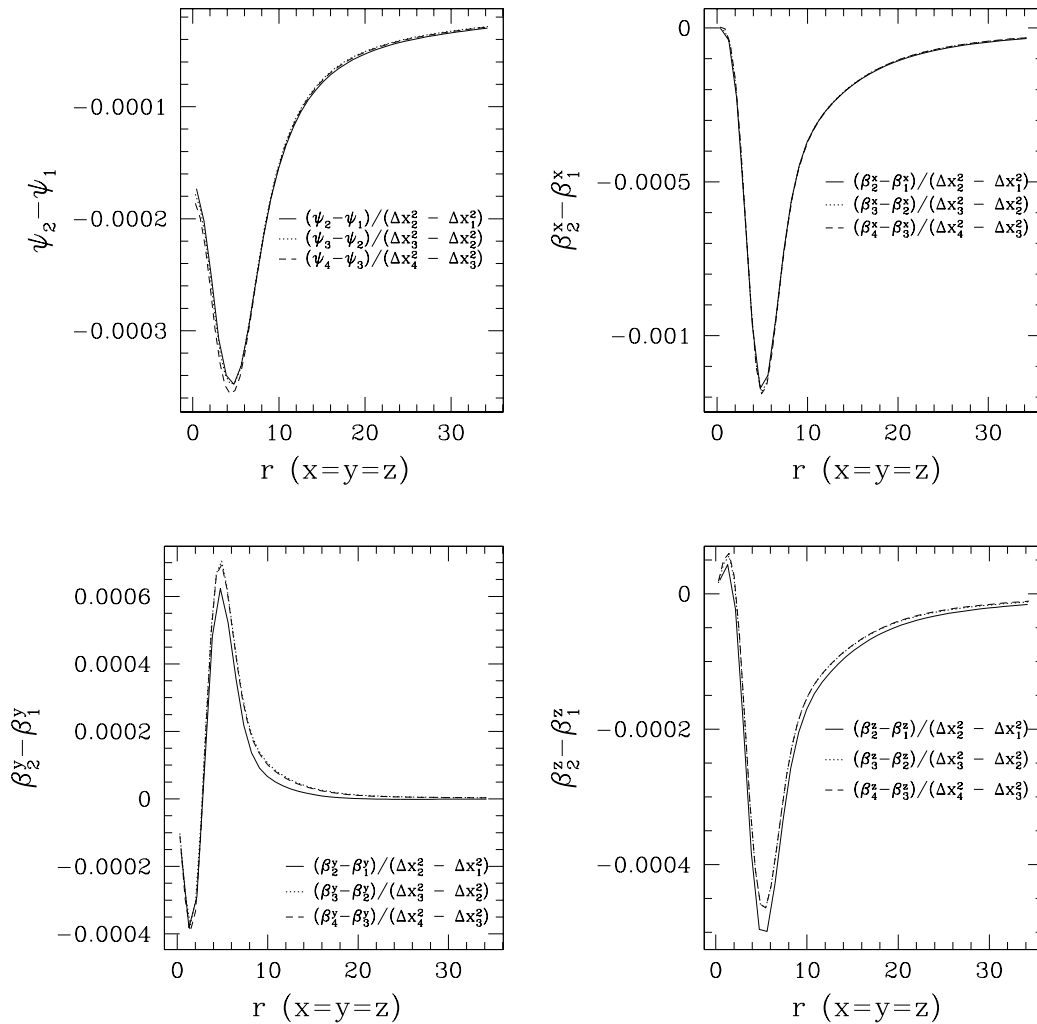


FIG. 3: Numerical convergence of the conformal factor  $\psi$  and the shift  $\beta^i$  for the PCT [28] binary configuration described in the text. We plot the rescaled differences between four different resolutions to establish second-order convergence (see Appendix F).

compare with their results for

$$\alpha\psi^{-6} = \alpha_A\alpha_B. \quad (55)$$

For this test we also adopt their boundary conditions (40). The implementation of PCT allows for imposing the outer boundary conditions (31) at a much larger separation than we can afford. Following PCT we construct a nonspinning black hole binary with background mass  $M = M_0$ , centers of the excised spheres at a coordinate separation  $d = 11.75M_0$ , and angular velocity  $\Omega = 0.0421/M_0$ . (According to the effective potential method in [4] this choice of  $\Omega$  corresponds to a circular orbit.)

In Fig. 3 we compare our results for the conformal factor  $\psi$  and the shift  $\beta^i$  for different resolutions (all with  $r_{\text{excision}} = 2.0M_0$ ), and again establish second-order convergence of our numerical code. In Table I we tabulate

both PCT's and our results for the binaries irreducible mass, the ADM mass, the angular momentum and the proper separation between the horizons. To compute the ADM mass and the angular momentum we extrapolate our numerical results to a grid with outer boundaries at  $150M_0$  as explained in Appendices A and C. We find values that are very similar to those found by PCT, but ours do not converge to theirs for a fixed location of the outer boundary. We believe that this is caused by the proximity of our outer boundary, and expect, as the results in Table I suggest, that the agreement would improve by increasing both the resolution and the distance to the outer boundaries. From Table I we estimate that the numerical errors in our results, given the grid resolution and location of the outer boundaries adopted in this paper, are of the order of about a percent.



$\Delta x/M$	Domain	$M_{\text{irr}}/M$	$M_{\text{ADM}}/M$	$J/M^2$	$\ell/M$
CTS		1.06528	2.08436	3.3790	10.3971
1/2	small	1.089	2.106	3.389	10.121
1/3	small	1.081	2.110	3.391	10.123
1/4	small	1.079	2.113	3.391	10.125
1/6	small	1.074	2.120	3.392	10.126
1/2	big	1.088	2.092	3.379	10.122
1/3	big	1.081	2.093	3.381	10.124
1/4	big	1.079	2.094	3.382	10.126
1/6	big	1.074	2.097	3.382	10.127

TABLE I: Comparison of our results with those of Pfeiffer, Cook and Teukolsky [28] for a binary with  $M = M_0$ ,  $d = 11.75M_0$  and  $\Omega = 0.0421/M_0$ . Here  $M$  is the mass parameter of both black holes,  $M_{\text{irr}}$  is the irreducible mass,  $M_{\text{ADM}}$  is the ADM mass,  $J$  is the angular momentum, and  $\ell$  is the proper distance between black hole horizons. Here a small boundary box refers to  $-20M \leq x \leq 20M$ ,  $0 \leq y \leq 20M$  and  $0 \leq z \leq 20M$ ; a large boundary box refers to  $-30M \leq x \leq 30M$ ,  $0 \leq y \leq 30M$  and  $0 \leq z \leq 30M$ .

Reference	$E_b/\mu$	$J/(2\mu M_{\text{irr}})$	$2\Omega M_{\text{irr}}$
Schwarzschild	-0.0572	3.464	0.068
[4]	-0.09030	2.976	0.172
[5]	-0.092	2.95	0.18
[7]	-0.068	3.36	0.103
[42]	-0.058	3.45	0.085
This work	-0.06	3	0.08
[54]	-0.0668	3.27	0.0883

TABLE II: Values for the binding energy  $E_b/\mu$ , the angular velocity  $2\Omega M_{\text{irr}}$  and the angular momentum  $J/(2\mu M_{\text{irr}})$  at the ISCO as obtained in different approaches. The Schwarzschild results refer to the innermost stable circular orbit of a test particle in a Schwarzschild spacetime. Our results for this work are determined from the turning point of the binding energy curve in Fig. 5; but, as discussed in the text, they are prone to large errors.

## B. An approximate inspiral sequence

We now proceed to construct an approximate inspiral sequence for a nonspinning black hole binary system, adopting the inner boundary conditions described in Section II D. Contours of the conformal factor  $\psi$ , the lapse  $\alpha$  and the shift  $\beta^i$  for one particular binary separation are shown in Fig. 4.

The binding energy of an equal mass binary can be defined as [4]

$$E_b = M_{\text{ADM}} - 2M_{\text{irr}}. \quad (56)$$

A simultaneous turning point in the binding energy and the angular momentum locates the ISCO. In Fig. 5 we show both the binding energy and the angular momentum. We show numerical results obtained with a resolution of  $\Delta x = M_0/4$  and with the outer boundary at  $30M_0$ , which corresponds to the highest resolution and largest grid run in our comparison in Section III A 2. The

code is run with the IBM pSeries 690 machine in NCSA. Each run with  $240 \times 120 \times 120$  gridpoints takes about 1600 cpu hours and uses about 8 giga bytes of memory. We set  $r_{\text{excision}} = 1.6M_0$  for these models. We also compare our results with the numerical results of: Cook [42], for an Eddington-Finkelstein slicing and  $d\alpha\psi/dr = 0$  inner boundary condition ([42]a), an Eddington-Finkelstein slicing and  $\alpha\psi = 1/2$  inner boundary condition ([42]b), and a maximal slicing and  $d\alpha\psi/dr = \alpha\psi/2r$  inner boundary condition ([42]c); with the binary initial data in [7]; with the second-order, post-Newtonian sequence in [4]; and with the third-order, post-Newtonian sequence in [29].

Our results for the binding energy agree fairly well with those of [42]b, while our results for the angular momentum do not. Note that we find a turning point in the binding energy, but not in the angular momentum. There are several possible reasons for these findings. Solving the constraints in the thin-sandwich decomposition leads to configurations that are in approximate equilibrium, but lacking dynamical evolutions, it is difficult to determine just how good this approximation is for this scenario [55]. Another potential reason for our findings are the inner boundary conditions (49), which may lead to undesirable deviations from quasi-equilibrium. Probably more important, however, is the limited numerical accuracy of our finite-difference, Cartesian code. From Table I we estimate that the accuracy of our values for the masses and angular momenta is of the order of a percent or so. From equation (56) the binding energy is computed as the difference between two masses, and is of the order of about 10 % of each of those masses (see Fig. 5). The relative error in this smaller difference is therefore significantly larger than the error in each of the terms separately, and may be as large as 10 % or more. Such an error is large enough to spoil the accuracy of an inspiral sequence. However, if taken at face value, the orbital parameters at the turning point of the binding energy agree fairly well with recent results for the binary black hole ISCO (see Table II).

While our results are not accurate enough to reliably locate the ISCO, we do believe that they are suitable for adoption as initial data in current dynamical evolution calculations in finite difference implementations. For these purposes, the accuracy of the initial data only needs to be as small as that of the dynamical evolution itself. The individual metric quantities that must be specified as initial data are not small differences of large numbers and are determined to about a percent.

We also note that solving the constraints in the Bowen-York formalism leads to higher accuracy solutions even in finite difference implementations (compare [5]). There, the momentum constraint can be solved analytically, leaving only the Hamiltonian constraint to be solved numerically. Moreover, the angular momentum can be determined analytically in terms of the background quantities. The Bowen-York formalism also adopts maximal slicing,  $K = 0$ , so that octant symmetry can be

adopted and a higher grid resolution can be chosen (compare Appendix E). In our approach, five coupled equations are solved simultaneously, and all orbital parameters are computed numerically from the solutions, which will clearly lead to a larger numerical error.

#### IV. DISCUSSION

We present a method for constructing solutions to the constraint equations of general relativity, describing quasi-equilibrium binary black holes in nearly circular orbit. We expect that these solutions are suitable initial data for dynamical evolution with current finite difference evolution codes.

We solve the constraint equations in a conformal thin-sandwich decomposition (e.g. [27]), and impose quasi-circular orbits by imposing that the ADM mass of the binary be equal to its Komar mass (compare [7]). We adopt a superposition of two Schwarzschild black holes in Kerr-Schild coordinates as the conformal background solution. This background choice leads to horizon-penetrating coordinates, which are needed for dynamical evolutions, and is likely to produce less spurious gravitational radiation, at least for rotating black holes. We present a new set of simple inner boundary conditions, to be imposed on the excision surface inside the black hole, which we hope leads to reasonable approximation to equilibrium (compare [30]).

We present two numerical tests – one for the limiting case of an isolated black hole, and the other for a binary configuration considered in [28]. We also construct an approximate inspiral sequence. Our numerical accuracy may not be sufficient to track the binding energy to high precision, since it is computed as the small difference between two significantly larger numbers. However, we do expect that our solutions provide adequate initial data for current finite-difference evolution codes. We also expect that when our formalism is implemented with higher resolution and/or more accurate numerical schemes, the inspiral sequence may provide a more reliable estimate of the ISCO parameters.

#### Acknowledgments

It is a pleasure to thank P. Marronetti and W. Tichy for useful discussions. This paper was supported in part by NSF Grants PHY-0090310 and PHY-0345151 and NASA Grant NNG04GK54G at the University of Illinois at Urbana-Champaign (UIUC) and by NSF Grant PHY-0139907 at Bowdoin College. Numerical calculations were carried out at the National Center for Super-computing Applications at UIUC.

#### APPENDIX A: THE ADM MASS INTEGRAL

Having conformally decomposed the spatial metric  $\gamma_{ij}$ , the ADM mass integral (51) can be written as

$$M_{\text{ADM}} = \frac{1}{16\pi} \oint_{\mathcal{S}_\infty} (\tilde{\Gamma}^i - \tilde{\Gamma}^{ji}{}_j - 8\tilde{\nabla}^i\psi)d\tilde{S}_i \quad (\text{A1})$$

where  $\tilde{\Gamma}^i \equiv \tilde{\gamma}^{lm}\tilde{\Gamma}^i{}_{lm}$  (compare [19]) and where  $\mathcal{S}_\infty$  is a closed surface at spatial infinity. For the background data described in Section IIB the first two terms can be evaluated analytically and yield the sum of the two background masses  $M_A + M_B$ , or, for equal mass binaries,  $2M_0$ . The ADM mass therefore reduces to

$$M_{\text{ADM}} = 2M_0 - \frac{1}{2\pi} \oint_{\mathcal{S}_\infty} \tilde{\nabla}^i\psi d\tilde{S}_i. \quad (\text{A2})$$

We now convert this surface integral into a volume integral using Gauss' law; volume integrals are typically more accurate numerically than surface integrals. However, since a volume, say  $V_1$ , containing a black hole singularity is excised, a surface integral over the surface of that volume, say  $\mathcal{S}_1$ , remains

$$\begin{aligned} M_{\text{ADM}} &= 2M_0 - \frac{1}{2\pi} \oint_{\mathcal{S}_\infty} \tilde{\nabla}^i\psi d\tilde{S}_i, \\ &= 2M_0 - \frac{1}{2\pi} \oint_{\mathcal{S}_1} \tilde{\nabla}^i\psi d\tilde{S}_i \\ &\quad - \frac{1}{2\pi} \int_{V_2+V_3+V_\infty} \sqrt{\tilde{\gamma}}\tilde{\nabla}^2\psi d^3x, \\ &= 2M_0 - \frac{1}{2\pi} \oint_{\mathcal{S}_1} \tilde{\nabla}^i\psi d\tilde{S}_i \\ &\quad + \frac{1}{16\pi} \int_{V_2+V_3+V_\infty} \sqrt{\tilde{\gamma}}[-\psi\tilde{R} \\ &\quad + \psi^{-7}\tilde{A}_{ij}\tilde{A}^{ij} - \frac{2}{3}\psi^5K^2]d^3x, \end{aligned} \quad (\text{A3})$$

Here we have used the Hamiltonian constraint in the third equality, and have denoted the volume outside  $V_1$  as  $V_2 + V_3 + V_\infty$  as illustrated in Fig. 6. Volume  $V_2$  denotes the space covered by our computational grid. Given our constraints on numerical grid resources, this volume extends only to a separation of typically  $30M_0$  from the black holes. Restricting the ADM integral (A3) to this volume would introduce a fairly large error. We therefore extend the integration to a larger volume  $V_3$ , in which the integrand is estimated by extrapolating  $\beta^i$ ,  $\alpha$ , and  $\psi$  from their values and fall-off conditions on the outer boundary of the computational grid  $\mathcal{S}_2$ :

$$\begin{aligned} \psi &\approx 1 + \frac{a_1}{r}, \\ \alpha &\approx 1 + \frac{a_2}{r}, \\ \beta^x &\approx \bar{\beta}^x + \frac{a_3y}{r^3}, \\ \beta^y &\approx \bar{\beta}^y + \frac{a_4x}{r^3}, \end{aligned} \quad (\text{A4})$$

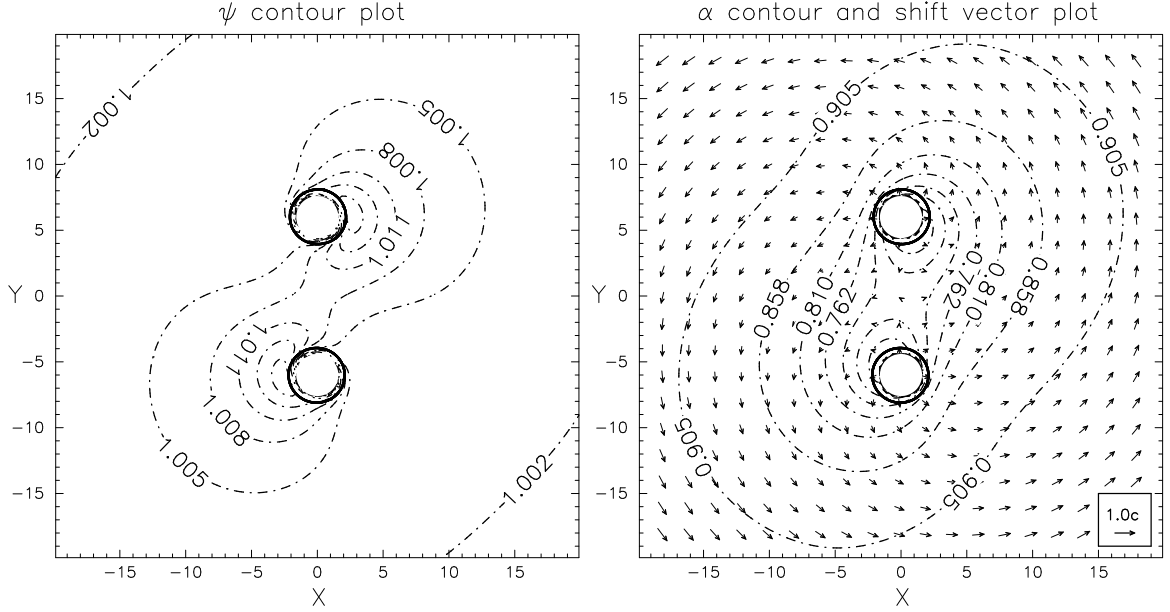


FIG. 4: The contour plots of the binary initial data with coordinate separation  $12M_0$ . The corresponding orbital velocity  $2\Omega M_{\text{irr}} = 0.0788$ . The left panel shows the contour of the conformal factor  $\psi$ ; the right panel shows the contour of lapse  $\alpha$  and the shift vector in the equatorial plane. The excision radius is  $1.6M_0$ . The two thick circles in the plots are the apparent horizons. The numerical value of the lapse  $\alpha$  on the apparent horizons exceeds 0.5 and is therefore positive, as required for horizon-penetrating coordinates. It is evident from the plots that the solutions do not satisfy octant symmetry (see Appendix E).

$$\beta^z \approx \bar{\beta}^z + \frac{a_5 z}{r^4}.$$

Here the  $a_i$  are coefficients that are determined as follows. For any point in  $V_3$ , say  $\vec{r}$ , we find the intersection of the position vector  $\vec{r}$  with  $S_2$ . The value of the function at that intersection determines the coefficient  $a_i$ . Once the coefficients  $a_i$  have been found, the functions  $\psi$ ,  $\alpha$  and  $\beta^i$  and hence the integrand of the ADM mass can be evaluated in  $V_3$  (compare [5]). Typically, the boundary of  $V_3$  is at a separation of  $150M_0$  from the black holes, so that this construction increases the volume of our integration by a factor of 125.

## APPENDIX B: THE KOMAR MASS INTEGRAL

The Komar mass can be defined for stationary, asymptotically flat spacetimes. Stationarity implies the existence of a Killing vector  $\xi^\nu$ , which can be written as

$$\xi^\nu = \alpha n^\nu + \beta^\nu, \quad (\text{B1})$$

where  $n_\mu \equiv -\alpha t_{,\mu}$  is the time-like unit normal on the spatial hypersurfaces  $\Sigma_t$ . The Komar mass is defined as

$$M_K = -\frac{1}{8\pi} \oint_{S_\infty} \xi^{[\mu;\nu]} dS_{\mu\nu} = -\frac{1}{4\pi} \oint_{S_\infty} \xi^{\mu;\nu} n_\mu dS_\nu, \quad (\text{B2})$$

where  $S_\infty$  is a closed hypersurface of  $\Sigma_t$ , diffeomorphic to a 2-sphere, at spatial infinity, and where we have used

Killing's equation  $\xi^{[\mu;\nu]} = \xi^{\mu;\nu}$ . The bi-vector  $dS_{\mu\nu} = 2n_{[\mu}dS_{\nu]}$ , where  $dS_\nu$  is a spatial oriented surface area element, is normal on both  $S_\infty$  and  $\Sigma_t$ . From (B1) we find

$$\xi^{\mu;\nu} n_\mu = -\alpha^{;\nu} + \beta^{\mu;\nu} n_\mu = -\alpha^{;\nu} - \beta^\mu n_{\mu}{}^{;\nu}. \quad (\text{B3})$$

Using the identity  $n_\mu{}^{;\nu} = -K_\mu{}^\nu - a_\mu n^\nu$ , where  $a_\mu \equiv n^\nu n_{\mu;\nu}$  is the 4-acceleration of normal observers, we obtain

$$\xi^{\mu;\nu} n_\mu dS_\nu = -(\alpha^{;\mu} - \beta^\nu K_\nu{}^\mu) dS_\mu. \quad (\text{B4})$$

Inserting this into (B2) yields

$$M_K = \frac{1}{4\pi} \oint_{S_\infty} (\nabla^i \alpha - \beta^j K_j{}^i) dS_i. \quad (\text{B5})$$

The term  $\beta^j K_j{}^i$  often falls off faster than  $1/r^2$  in an asymptotically flat space, in which case its contribution to the integral vanishes. Here, however, this term must be retained.

The Komar mass is independent of the surface  $S$  on which the integral is evaluated, as long as all matter sources are inside of  $S$ . To demonstrate this, we convert the surface integral in (B5) into the volume integral

$$M_K = \frac{1}{4\pi} \int (\nabla_i \nabla^i \alpha - \beta^j \nabla^i K_{ij} - K_{ij} \nabla^i \beta^j) \sqrt{\gamma} d^3x. \quad (\text{B6})$$

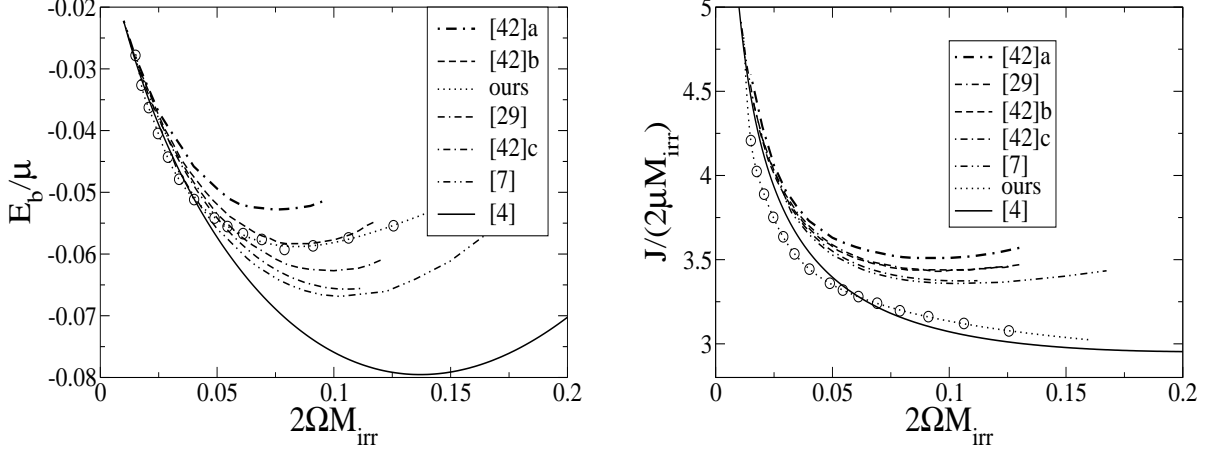


FIG. 5: The binding energy  $E_b$  and angular momentum  $J$  as a function of orbital angular velocity. The dotted lines are least square fits to our numerical results, marked by open circles. We compare with thin-sandwich results in [42] for an Eddington-Finkelstein slicing and  $d\alpha\psi/dr = 0$  inner boundary condition ([42]a), an Eddington-Finkelstein slicing and  $\alpha\psi = 1/2$  inner boundary condition ([42]b), and a maximal slicing and  $d\alpha\psi/dr = \alpha\psi/2r$  inner boundary condition ([42]c), with the binary initial data in [7], with the second-order, post-Newtonian sequence in [4], and with the third-order, post-Newtonian sequence in [29]. Here  $\mu$  is the reduced mass ( $M_{\text{irr}}/2$ ) and  $M_{\text{irr}}$  is the irreducible mass for one black hole.

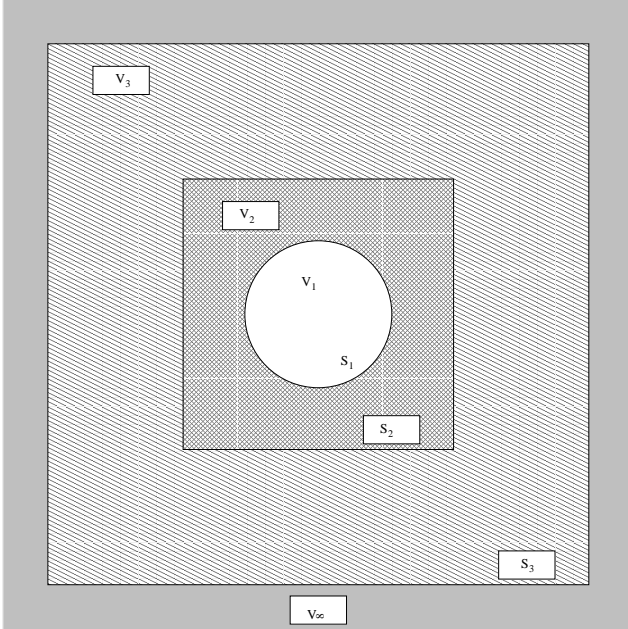


FIG. 6: The diagram illustrates the relation between the volumes  $V_1$ ,  $V_2$ , and  $V_3$  and the surfaces  $S_1$ ,  $S_2$ , and  $S_3$ .  $S_1$  is a boundary outside both black holes, but well inside the computational domain,  $S_2$  is a boundary near the outer edge of the computational domain, and  $S_3$  is a boundary well outside the computational domain (at very large, finite radius).

This integral can be rewritten by inserting the trace of

the evolution equation (5)

$$\nabla_i \nabla^i \alpha = \alpha \left( K_{ij} K^{ij} + \frac{1}{2}(\rho + s) \right) + \beta^i \nabla_i K - \partial_t K, \quad (\text{B7})$$

and the momentum constraint (3)

$$\nabla^j K_{ij} = \nabla_i K + s_i, \quad (\text{B8})$$

where, for completeness, we have included the matter sources  $\rho$ ,  $s_i$  and  $s$

$$\begin{aligned} \rho &= n_\mu n_\nu T^{\mu\nu}, \\ s_i &= -\gamma_{i\mu} n_\nu T^{\mu\nu}, \\ s &= \delta^i_\mu \gamma_{i\nu} T^{\mu\nu}. \end{aligned} \quad (\text{B9})$$

The volume integral (B6) then becomes

$$\begin{aligned} M_K &= \frac{1}{4\pi} \int \sqrt{\gamma} d^3x \left\{ \alpha \left( K_{ij} K^{ij} + \frac{1}{2}(\rho + s) \right) \right. \\ &\quad \left. - \partial_t K - K_{ij} \nabla^i \beta^j - \beta^i s_i \right\}. \end{aligned} \quad (\text{B10})$$

We now use the evolution equation (4) to rewrite the term  $K_{ij} \nabla^i \beta^j$  as

$$K_{ij} \nabla^i \beta^j = \alpha K_{ij} K^{ij} + \frac{1}{2} K^{ij} \partial_t \gamma_{ij}. \quad (\text{B11})$$

This brings the integral (B10) into the form

$$\begin{aligned} M_K &= \frac{1}{4\pi} \int \sqrt{\gamma} d^3x \left( \frac{1}{2} \alpha (\rho + s) - \beta^i s_i \right. \\ &\quad \left. - \partial_t K - \frac{1}{2} K^{ij} \partial_t \gamma_{ij} \right). \end{aligned} \quad (\text{B12})$$

As in the calculation of the ADM mass, part of the numerical grid may have to be excluded from the integration, for example if it contains a black hole singularity. The integral over an outer surface  $\mathcal{S}_\infty$  can then be written as a volume integral  $V$  and a surface integral over an inner surface, e.g.  $\mathcal{S}_1$  as in Fig 6

$$\begin{aligned} M_K &= \frac{1}{4\pi} \oint_{\mathcal{S}_\infty} (\nabla^i \alpha - \beta^j K_j^i) dS_i \\ &= \frac{1}{4\pi} \int_{V_2+V_3+V_\infty} \sqrt{\gamma} d^3x \left( \frac{1}{2} \alpha (\rho + s) - \beta^i s_i \right. \\ &\quad \left. - \partial_t K - \frac{1}{2} K^{ij} \partial_t \gamma_{ij} \right) \\ &\quad + \frac{1}{4\pi} \oint_{\mathcal{S}_1} (\nabla^i \alpha - \beta^j K_j^i) dS_i. \end{aligned} \quad (\text{B13})$$

From the above assumption of stationarity, the time derivatives of  $\gamma_{ij}$  and  $K$  have to vanish, and as long as there are no matter sources in  $\Omega$ ,  $\rho = s = s_i = 0$ , the volume integral vanishes and we have

$$\frac{1}{4\pi} \oint_{\mathcal{S}_1} (\nabla^i \alpha - \beta^j K_j^i) dS_i = \frac{1}{4\pi} \oint_{\mathcal{S}_\infty} (\nabla^i \alpha - \beta^j K_j^i) dS_i \quad (\text{B14})$$

(compare [57]).

### APPENDIX C: THE ANGULAR MOMENTUM INTEGRAL

In Cartesian coordinates, the angular momentum can be defined as

$$J_i = \frac{1}{8\pi} \epsilon_{ij}{}^k \oint_{\mathcal{S}_\infty} x^j K^\ell{}_k d^2 S_\ell \quad (\text{C1})$$

(see [23, 46]). In this paper we only consider rotations about the  $z$ -axis, and therefore compute only the  $z$ -component of the angular momentum which can be rewritten as

$$\begin{aligned} J_z &= \frac{1}{8\pi} \oint_{\mathcal{S}_\infty} (x \tilde{A}^l{}_y - y \tilde{A}^l{}_x) d\tilde{S}_l, \\ &= \frac{1}{8\pi} \oint_{\mathcal{S}_1} (x \tilde{A}^l{}_y - y \tilde{A}^l{}_x) d\tilde{S}_l \\ &\quad + \frac{1}{8\pi} \int_{V_2+V_3+V_\infty} \left( \tilde{A}^x{}_y + \frac{2}{3} \psi^6 x \tilde{\nabla}_y K \right. \\ &\quad \left. - \frac{1}{2} x \tilde{A}_{ij} \partial_y \tilde{\gamma}^{ij} - \tilde{A}^y{}_x - \frac{2}{3} \psi^6 y \tilde{\nabla}_x K \right. \\ &\quad \left. + \frac{1}{2} y \tilde{A}_{ij} \partial_x \tilde{\gamma}^{ij} \right) \sqrt{\tilde{\gamma}} d^3x. \end{aligned} \quad (\text{C2})$$

As in the calculation of the ADM mass (Appendix A) we have converted the surface integral into a volume integral for greater numerical accuracy. As before, we evaluate the integral from the numerical data in volume  $V_2$  and from extrapolated values in volume  $V_3$ . We neglect only those contributions to the integral from volume  $V_\infty$ .

### APPENDIX D: INERTIAL AND ROTATING FRAMES

Rotating frames are not asymptotically flat, so that the expressions for the ADM (Appendix A), angular momentum (Appendix C) and Komar mass (Appendix B) have to be re-evaluated.

The barred coordinates  $\bar{t}$ ,  $\bar{x}$ ,  $\bar{y}$  and  $\bar{z}$  in an inertial frame are related to the unbarred coordinates  $t$ ,  $x$ ,  $y$  and  $z$  in a rotating frame by the transformation

$$\begin{aligned} \bar{t} &= t, \\ \bar{x} &= x \cos(\omega t) - y \sin(\omega t), \\ \bar{y} &= x \sin(\omega t) + y \cos(\omega t), \\ \bar{z} &= z. \end{aligned} \quad (\text{D1})$$

Here we are assuming a constant angular velocity  $\vec{\omega} = (0, 0, \omega)$  and rotation about the  $z$ -axis. At an arbitrary instant  $\bar{t} = t = 0$  at which the two frames are aligned the gravitational field variables are related by [56]

$$\begin{aligned} \alpha &= \bar{\alpha}, \\ \beta^i &= \bar{\beta}^i + (\vec{\omega} \times \vec{r})^i, \\ \gamma_{ij} &= \bar{\gamma}_{ij}, \\ K_{ij} &= \bar{K}_{ij}, \end{aligned} \quad (\text{D2})$$

The only effect of this transformation is therefore the appearance of a new term in the shift. Since the shift does not enter the integrals for the ADM mass nor the angular momentum, those quantities remain unchanged and we only have to re-evaluate the Komar mass.

Transforming between the rotating and inertial frame, we find that the Komar mass in the rotating frame  $M_K$  is related to that in the inertial frame  $\bar{M}_K$  by

$$\begin{aligned} M_K &= \frac{1}{4\pi} \oint (\nabla^i \alpha - \beta^j K_j^i) dS_i \\ &= \frac{1}{4\pi} \oint (\nabla^i \bar{\alpha} - \bar{\beta}^j \bar{K}_j^i) d\bar{S}_i - \frac{1}{4\pi} \oint (\vec{\omega} \times \vec{r})^j \bar{K}_j^i d\bar{S}_i \\ &= \bar{M}_K - \frac{\omega}{4\pi} \epsilon^j{}_{z\ell} \oint x^\ell \bar{K}_j^i d\bar{S}_i \\ &= \bar{M}_K - 2\omega J \end{aligned} \quad (\text{D3})$$

(note that the angular momentum is the same in both frames, so  $\bar{J} = J$ ).

### APPENDIX E: SYMMETRIES OF THE COMPUTATIONAL DOMAIN

Symmetries can be used to reduce the size of the computational grid, making it desirable to incorporate as many symmetries as possible. One might expect that the binary black hole configuration studied in this paper would allow for octant symmetry. In this Appendix we show that this is not the case, due to the presence of a non-zero trace of the extrinsic curvature (i.e. non-maximal slicing).

Consider, for example, the momentum constraint (3) and assume, for simplicity, conformal flatness. On the  $x = 0$  plane, it would be natural to assume that  $\beta^x$  be symmetric, while  $\beta^y$  and  $\beta^z$  be anti-symmetric (compare, for example, [39]). Computing  $\tilde{A}^{ij}$  from the shift according to (12), assuming that all scalars are symmetric on all coordinate planes, shows that  $\tilde{A}^{xx}$ ,  $\tilde{A}^{yy}$ ,  $\tilde{A}^{zz}$  and  $\tilde{A}^{xy}$  are all anti-symmetric on the  $x = 0$  plane, while  $\tilde{A}^{xy}$  and  $\tilde{A}^{xz}$  are symmetric. The divergence  $\nabla_i \tilde{A}^{xi}$ , for example, is then symmetric on the  $x = 0$  plane. The gradient  $\nabla^i K$ , however, must be anti-symmetric, meaning that the momentum constraint (3) violates this symmetry assumption. Similar arguments hold on the  $y = 0$  plane. Under the assumption of maximal slicing  $K = 0$ , octant symmetry can be adopted, but in this paper we adopt a Kerr-Schild background with  $K \neq 0$ . The above issue does not apply on the  $z = 0$  plane, so that equatorial symmetry can be assumed even in the non-maximal slicing case  $K \neq 0$ .

It is possible, however, to adopt  $\pi$ -symmetry, whereby

$$f(-x, -y, z) = \sigma f(x, y, z). \quad (\text{E1})$$

For scalar functions we have  $\sigma = 1$ , while for the  $x$ ,  $y$  and  $z$ -component of the shift we have  $\sigma_x = -1$ ,  $\sigma_y = -1$ , and  $\sigma_z = 1$ , respectively.

## APPENDIX F: SECOND-ORDER CONVERGENCE

Second-order convergence is most easily demonstrated by doubling the computational grid resolution several

times and showing that numerical errors scale in the expected way. Given the constraints of computational resources it is often impossible to double the grid size several times, so instead we establish second-order convergence by considering three arbitrary (but different) grid spacings  $h_1$ ,  $h_2$ , and  $h_3$ .

Let  $Q(h)$  be a quantity obtained from a finite difference scheme with spacing  $h$ . A Taylor expansion around  $h = 0$  yields

$$\begin{aligned} Q(h) &= Q(0) + h \left. \frac{\partial Q}{\partial h} \right|_{h=0} + \frac{h^2}{2} \left. \frac{\partial^2 Q}{\partial h^2} \right|_{h=0} + O(h^3) \\ &\equiv Q_0 + Q_1 h + Q_2 h^2 + O(h^3). \end{aligned} \quad (\text{F1})$$

Second-order convergence implies that  $Q_1 = 0$ . Given two different resolutions  $h_1$  and  $h_2$  we can eliminate  $Q_0$  and find

$$Q_2 = \frac{Q(h_2) - Q(h_1)}{h_2^2 - h_1^2} + O(h). \quad (\text{F2})$$

Alternatively,  $Q_2$  can be computed from the two grid spacings  $h_2$  and  $h_3$ . Second-order convergence can then be established by showing that the differences between different values for  $Q_2$  decrease at least as fast as  $h$ .

- 
- [1] A. Buonanno and T. Damour, *Phys. Rev. D* **59**, 084006 (1999); A. Buonanno and T. Damour, *Phys. Rev. D* **62**, 064015 (2000); T. Damour, *Phys. Rev. D* **64**, 124013 (2001).
  - [2] T. W. Baumgarte & S. L. Shapiro, *Phys. Rep.* 376 41 (2003).
  - [3] G. B. Cook, *Living Reviews in Relativity* **3**, 2000-5 (2000) (<http://www.livingreviews.org/>).
  - [4] G. B. Cook, *Phys. Rev. D* **50**, 5025 (1994).
  - [5] T. W. Baumgarte, *Phys. Rev. D* **62**, 024018 (2000)
  - [6] E.ourgoulhon, P. Grandclement, & S. Bonazzola, *Phys. Rev. D* **65**, 044020 (2002).
  - [7] P. Grandclement, E.ourgoulhon, & S. Bonazzola, *Phys. Rev. D* **65**, 044021 (2002).
  - [8] H. P. Pfeiffer, S. A. Teukolsky, & G. B. Cook, *Phys. Rev. D* **62** 104018 (2000).
  - [9] B. D. Baker, gr-qc/0205082 (2002).
  - [10] W. Tichy & Bernd Brügmann, *Phys. Rev. D* **69**, 024006 (2004).
  - [11] M. Ansorg, B. Brügmann & W. Tichy, submitted (see also gr-qc/0404056).
  - [12] B. Brügmann, *Int. J. Mod. Phys. D* **8**, 85 (1999).
  - [13] S. Brandt, R. Correll, R. Gómez, M. Huq, P. Laguna, L. Lehner, P. Marronetti, R.A. Matzner, D. Neilsen, J. Pullin, E. Schnetter, D. Shoemaker, & J. Winicour, *Phys. Rev. Lett.* **85**, 5496 (2000).
  - [14] M. Alcubierre, W. Bengert, B. Brügmann, G. Lanfermann, L. Neger, E. Seidel, & R. Takahashi, *Phys. Rev. Lett.* **87** 271103 (2001).
  - [15] J. Baker, B. Brügmann, M. Campanelli, C. O. Lousto, & R. Takahashi, *Phys. Rev. Lett.* **87**, 121103 (2001).
  - [16] B. Brügmann, W. Tichy & N. Jansen, *Phys. Rev. Lett.*, in press (2004).
  - [17] M. Shibata & T. Nakamura, *Phys. Rev. D* **52**, 5428 (1995).
  - [18] T.W. Baumgarte & S.L. Shapiro, *Phys. Rev. D* **59**, 024007 (1999).
  - [19] H.J. Yo, T.W. Baumgarte, & S.L. Shapiro, *Phys. Rev. D* **66**, 084026 (2002).
  - [20] M. Alcubierre & B. Brügmann, *Phys. Rev. D* **63** 104006 (2001).
  - [21] R.A. Matzner, M.F. Huq, & D. Shoemaker, *Phys. Rev. D* **59**, 024015 (1999).
  - [22] P. Marronetti & R.A. Matzner, *Phys. Rev. Lett.* **85**, 5500

- (2000).
- [23] J.M. Bowen & J.W. York, Jr., *Phys. Rev. D*, **21**, 2047, (1980).
- [24] W. Tichy, B. Brügmann, & P. Laguna, *Phys. Rev. D* **68** 064008 (2003).
- [25] M.D. Hannam, C.R. Evans, G.B. Cook, & T.W. Baumgarte, *Phys. Rev. D* **68** 064003 (2003).
- [26] J.R. Wilson, & G.J. Mathews, in Evans et al. eds., *Frontiers in Numerical Relativity*, 306-314, (Cambridge Univ. Press, Cambridge, England, 1989).
- [27] J.W. York, Jr., *Phys. Rev. Lett.* **82**, 1350, (1999).
- [28] H.P. Pfeiffer, G.B. Cook, & S.A. Teukolsky, *Phys. Rev. D* **66** 024047 (2002).
- [29] T. Damour, E. Gourgoulhon, P. Grandclément, *Phys. Rev. D* **66** 024007 (2002).
- [30] G.B. Cook, *Phys. Rev. D* **65** 084003 (2002).
- [31] S. Brandt & B. Brügmann, *Phys. Rev. Lett.* **78**, 3606, (1997).
- [32] M. L. Skoge & T. W. Baumgarte, *Phys. Rev. D* **66**, 107501 (2002).
- [33] A. Lichnerowicz, *J. Math. Pure Appl.* **23**, 37 (1744).
- [34] J.W. York, Jr., in *Sources of Gravitational Radiation*, edited by L.L. Smarr (Cambridge Univ. Press, Cambridge, England, 1979), pp. 83.
- [35] J.W. York, Jr., *J. Math. Phys.*, **14**, 456, (1973).
- [36] J.W. York, Jr., *Ann. Inst. Henri Poincaré A* **21**, 319 (1974).
- [37] G.B. Cook, S.L. Shapiro, & S.A. Teukolsky, *Phys. Rev. D* **53**, 5533 (1996).
- [38] E. Gourgoulhon & S. Bonazzola, *Class. Quantum Grav.* **11**, 443 (1994).
- [39] T.W. Baumgarte, G.B. Cook, M.A. Scheel, S.L. Shapiro, & S.A. Teukolsky, *Phys. Rev. D* **57** 7299 (1998).
- [40] A. Ashtekar, C. Beetle, O. Dreyer, S. Fairhurst, B. Krishnan, J. Lewandowski, & J. Wisniewski, *Phys. Rev. Letters* **85**, 3564 (2000).
- [41] H.P. Pfeiffer, Ph.D. thesis, (2003).
- [42] G.B. Cook, talk presentation in ITP, Santa Barbara, [http://online.kitp.ucsb.edu/online/gravity\\_c03](http://online.kitp.ucsb.edu/online/gravity_c03) (2003). See also G.B. Cook and H.P. Pfeiffer, gr-qc/0407078.
- [43] A. Komar, *Phys. Rev.* **113**, 934 (1959).
- [44] R. Beig, *Phys. Lett.* **69A**, 153 (1978).
- [45] A. Ashtekar & A. Magnon-Ashtekar, *J. Math. Phys.* **20**, 793 (1979).
- [46] N.Ó. Murchadha & J.W. York, Jr., *Phys. Rev. D* **10**, 2345 (1974).
- [47] E. Bonning, P. Maronetti, D. Neilsen, and R. Matzner, *Phys. Rev. D* **68**, 044019 (2004).
- [48] In their recent preprint J. L. Jaramillo, E. Gourgoulhon, and G. A. Mena Marugan (submitted, 2004, also gr-qc/0407063) present a very similar inner boundary condition for the conformal factor.
- [49] D. Christodoulou, *Phys. Rev. Lett.* **25**, 1596 (1970).
- [50] J.D. Bekenstein, *Phys. Rev. D* **7**, 2333 (1973).
- [51] C.W. Misner, K.S. Thorne, & J.A. Wheeler. *Gravitation* (Freeman, New York, 1973).
- [52] K. Alvi, *Phys. Rev. D* **64**, 104020 (2001).
- [53] In this paper we do not employ scaling to avoid the iteration for  $M_{\text{irr}}$  as for example in eqns (79)-(82) in [7]. Unlike [7, 42] we do not impose the inner boundary conditions on the apparent horizon, so that scaling would change the location of the excision radius with respect to the apparent horizon. This behavior would complicate testing for convergence, as well as comparisons of data from different runs, so that we decided not to use scaling for the calculations presented in this paper.
- [54] T. Damour, P. Jaranowski, & G. Schafer, *Phys. Rev. D* **62**, 084011 (2000).
- [55] Different decompositions of the constraint equations and different choices of the freely specifiable variables lead to physically distinct initial data, which may contain different amounts of spurious gravitational radiation. This radiation can be measured by means of dynamical simulations, without which evaluations and comparisons of competing QE solutions remain imprecise (compare S. Dain, submitted (also gr-qc/0406099)).
- [56] M. Duez, P. Marronetti, S. L. Shapiro, & T. W. Baumgarte, *Phys. Rev. D* **67** 024004 (2003).
- [57] S. Detweiler, in *Frontiers in Numerical Relativity*, ed. C.R. Evans, L.S. Finn, & D.W. Hobill (Cambridge Univ. Press, Cambridge, 1989).